



Trans. Nonferrous Met. Soc. China 33(2023) 3885–3898

Transactions of Nonferrous Metals Society of China

www.tnmsc.cn



# Preparation of lightweight and high-strength ceramsite from highly doped coal fly ash

Li-sha WANG<sup>1,2</sup>, Yan-xiu WANG<sup>1,2</sup>, Wei SUN<sup>1,2</sup>, Cheng-wen WANG<sup>1,2</sup>, Xiang-song MENG<sup>1,2</sup>

 School of Minerals Processing and Bioengineering, Central South University, Changsha 410083, China;
Key Laboratory of Hunan Province for Clean and Efficient Utilization of Strategic Calcium-containing Mineral Resources, Changsha 410083, China

Received 11 April 2022; accepted 5 December 2022

**Abstract:** A method for producing lightweight and high-strength ceramsite from coal fly ash was presented. It provides a potential solution to the problem of coal fly ash stockpiling and makes effective use of SiO<sub>2</sub>, Al<sub>2</sub>O<sub>3</sub> and other substances. Based on the thermodynamic analysis, an optimized method for the preparation of lightweight high-strength ceramsite by sintering at high coal fly ash doping (60%–90%, mass fraction) was designed. The mineral transformation in the complex silicate systems was studied. The cooling method, the roasting process and the raw material formula were improved. At the roasting temperature of 1200 °C and the holding time of 5 min, the density of the ceramsite produced was less than 0.93 g/cm<sup>3</sup> and the strength was as high as 1.08 kN. The specific strength of ceramsite produced by this approach was significantly higher than that of several randomly purchased ceramsite products in the market. **Key words:** thermodynamics; mineral transition; process control; solid waste utilization; ceramsite; coal fly ash

### 1 Introduction

Coal fly ash is powdery dust produced by coal combustion at high temperatures. As solid waste, coal fly ash is generally formed by the loss of organic matter and water during combustion [1–3]. The yield depends on the degree of coal densification to a large extent. The higher the metamorphism degree of coal is, the higher the content of coal fly ash formed by combustion is [4,5]. In recent years, with the rapid development of industry, the emission of coal fly ash has increased significantly. In 2021, the emission of coal fly ash in China exceeded 750×106t, and the total coal fly ash reserves exceeded 3 billion tons [6,7]. The long-term stockpiling reaction results in the production of harmful gases, such as SO<sub>2</sub>, SO<sub>3</sub> and P [8-10], which will eventually harm

both the environment and human life. For instance, the accumulation of coal fly ash occupies the land, and the infiltration of heavy metals in coal fly ash contaminates land and groundwater resources, producing haze and fog, and even causing geological disasters [11–14]. The efficient use of coal fly ash to improve the treatment of industrial solid waste presents researchers with both a significant challenge and a fantastic opportunity.

In 2020, the output of ordinary ceramsite in China increased from 10.972×10<sup>6</sup> cm<sup>-3</sup> in 2019 to 11.478×10<sup>6</sup> cm<sup>-3</sup>, an increase of 4.6% annually [15]. The production of one ton of ceramsite requires the addition of approximately 0.40–0.58 t of coal fly ash [4,16–20]. Consequently, creating environment-friendly ceramsite from coal fly ash is an effective way to realize recycling resources. Preparing environment-friendly ceramsite with coal fly ash has been widely developed. Numerous studies have

discussed the use of coal fly ash to convert waste into treasure. Agriculture, construction, environmental protection, and other industries all heavily rely on coal fly ash, and these sectors are crucial to the full use of coal fly ash as a resource [8,21-23]. QIN et al [4] and LUO et al [6] proposed that the preparation of ceramsite from coal fly ash is not only an effective alternative to natural raw material extraction but also provides a new highperformance product. The ratio of silicon to aluminum is of considerable importance in the preparation of ceramsite from coal fly ash. To investigate the variables influencing performance researchers of ceramsite. established the reference of raw materials by a series of tests, including XRD and SEM. The optimal formula and process were identified and used to prepare ceramsite products with excellent performance and high feasibility [1,2,24]. YAO et al [25] and WANG et al [26] investigated the effects of sintering temperature and the quantity of pore-forming agents on the compressive strength, apparent porosity, water absorption, and water penetration of ceramsite.

The prepared porous ceramsite exhibits excellent physical and chemical properties. To explore the effect of pore-forming agent dosage and sintering temperature on the performance of coal fly ash porous ceramsite, WU et al [27] investigated the adsorption of Cr (VI) on porous ceramsite before and after modification. After alteration, the saturation adsorption capacity of porous ceramsite was noticeably high, indicating that the adsorption effect was outstanding. Under the condition that the utilization rate of coal fly ash is about 44%, GAO et al [28] reported that the addition of auxiliary materials, such as clay, provided effective support for the preparation of ceramsite containing large amounts of coal fly ash. In addition to addressing pollution concerns, the efficient use of coal fly ash for the preparation of ceramsite also solves the scarcity of ceramsite raw materials [18,23,29,30]. Despite studies on the use of coal fly ash to make ceramsite, solving the contradiction between the amount of coal fly ash and the ceramsite firing effect remains difficult. It is difficult to achieve large-scale solid waste utilization if only a small quantity of coal fly ash is used in the auxiliary, and the cost of production will rise dramatically due to the extensive transit of other raw materials.

In this study, the iterative optimization of the ceramsite formula and production process was conducted based on the thermodynamic analysis and mineral transformation of SiO2-Al2O3-Fe2O3-CaO-K2O complex silicate system and following the rule of minimizing external additives and the product defects of each time. The lightweight and high-strength ceramsite with equally distributed interior pores was manufactured. Factsage software was used for thermodynamics estimation and theoretical calculation of the ceramsite preparation process. Moreover, the properties of ceramsite were characterized, including its microscopic morphology and phase composition. By efficiently using valuable resources, our research helps to reduce the environmental impact of industrial solid waste.

### 2 Experimental

### 2.1 Testing of raw materials

The raw material of coal fly ash used for ceramsite preparation was collected from coal fly ash in the southern part of the Shuicheng Power Plant (Liupanshui, Guizhou Province, China). Bentonite, potassium feldspar and quartz powder (99% purity) were added as auxiliary ingredients to increase the contents of SiO<sub>2</sub> and Al<sub>2</sub>O<sub>3</sub> in ceramsite and compensate for the deficiency of the chemical composition of coal fly ash. As illustrated in Fig. 1(a), the main mineral components of coal fly ash are quartz, hematite, and mullite, while quartz and sanidine compose the majority of the clay minerals, bentonite and potassium feldspar. In general, quartz accounts for the largest proportion of the three raw materials, followed by sanidine. As shown in Fig. 1(b), the particle size distribution of the raw materials is fairly broad. Coal fly ash and potash feldspar contain coarser granules than quartz and bentonite, which have finer grains. The  $D_{50}$  of coal fly ash, quartz, bentonite, and potassium feldspar was 18.139, 11.703, 16.445, and 38.276 µm, respectively.

In Table 1, quantitative analysis results of the main chemical components of coal fly ash are presented. The chemical compositions of bentonite and potassium feldspar are listed in Table 2.

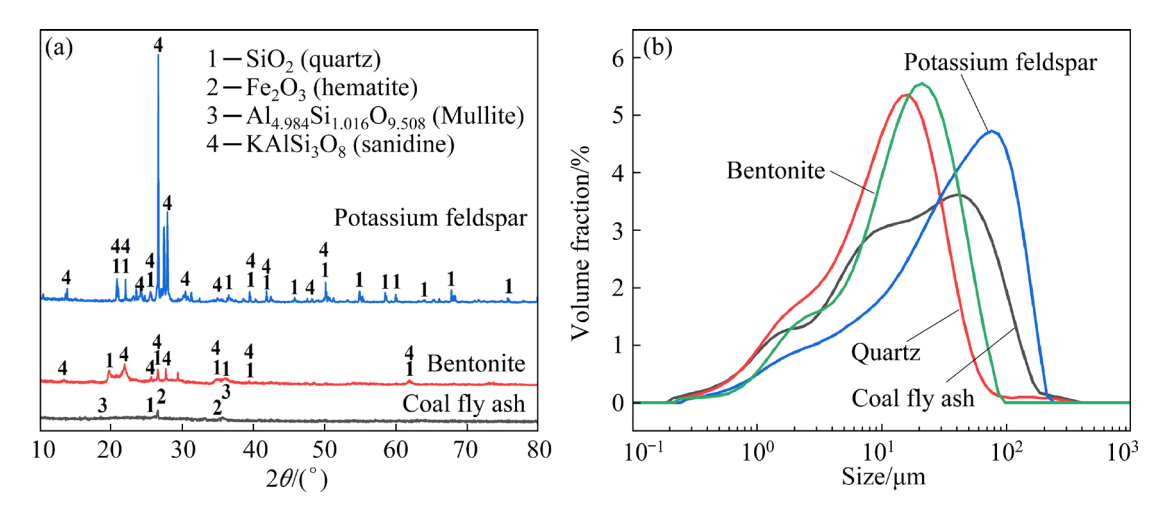


Fig. 1 XRD patterns (a) and particle size distribution (b) of raw materials

**Table 1** Chemical composition of partial coal fly ash (wt.%)

Fe <sub>2</sub> O <sub>3</sub>	SiO <sub>2</sub>	$Al_2O_3$	CaO	MgO	K <sub>2</sub> O	Na <sub>2</sub> O	С	LOI	Others
13.49	46.34	20.74	2.42	1.14	1.63	1.74	4.08	0.31	8.11

**Table 2** Main chemical contents of excipients (wt.%)

Excipient	$SiO_2$	$Al_2O_3$	$Fe_2O_3$	CaO	MgO	$K_2O$	Na <sub>2</sub> O	C	LOI	Others
Bentonite	51.00	33.50	_	-	-	3.21	-	0.31	0.56	11.42
Potassium feldspar	61.06	15.45	1.08	0.23	0.33	8.45	2.43	0.03	0.02	10.92

### 2.2 Test method

For reserves, coal fly ash was dried and disintegrated into a fine powder that was less than 0.150 mm. Pure quartz, potassium feldspar powder, and bentonite with a particle size of 0.074 mm were purchased from the market. According to the formula, the basic components were dry-mixed, and then 8%-10% water was added. The powder was mixed evenly and made into a sphere with a diameter of about 1 cm. The sample was preheated at 400 °C for around 30 min before being dried at 105 °C for 2-3 h. In a 12 kW lifting molybdenum rod furnace, temperature control techniques were designed following several fire systems. After ceramsite was burned at the maximum temperature of 1200 °C, it was cooled to room temperature before testing. Additionally, the formula and process were continuously optimized according to the test strength and density index with repeated iterations.

According to Fig. 2, the formulas and processes of this study are numbered as follows. The five formulas with different ingredients are

represented by A, B, C, D and E, while the modified optimized processes are represented by 0, 1, 2, 3 and 4. Thus, the formula and process represent a sample.

### 2.3 Detection and sample characterization

The chemical composition of coal fly ash was determined by a PANalytical Axios MAX dispersive X-ray wavelength fluorescence spectrometer. The main chemical components of Fe<sub>2</sub>O<sub>3</sub>, SiO<sub>2</sub>, Al<sub>2</sub>O<sub>3</sub>, CaO, MgO, K<sub>2</sub>O and Na<sub>2</sub>O were quantified by the glass melting standard curve method. The standard curves for each parameter were calibrated with standard samples ranging from 10 to 30 points. The concentration of the standard sample ranged from 0.005% to 80%. The error ranged between the measurement results, and that of the standard sample was less than 0.2%. By using a fast full-scan analysis, other minor elements were semi-quantitatively examined. The phase transitions and chemical reactions during sintering and cooling were analyzed by Factsage thermodynamic calculation software. The phase of the

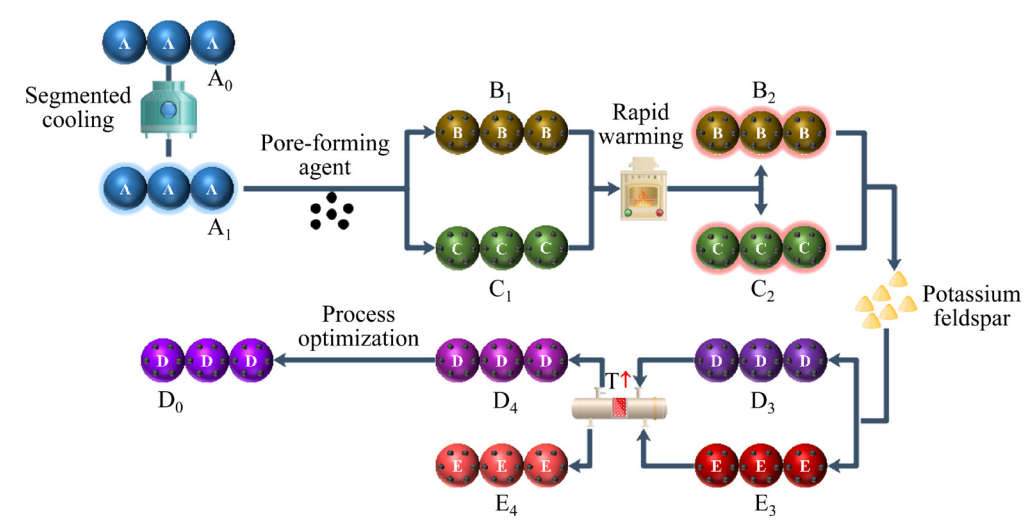


Fig. 2 Flow chart of formula and process optimization

solid samples was determined by a PANalytical X-Pert Powder Type X-ray diffractometer (Cu target, K<sub>a</sub> wavelength 0.15406 nm, working voltage 40 kV, working current 40 mA, step size 0.02°, scanning speed 8 (°)/min, scanning range 5°-80°). The diffraction curves were analyzed using X'pert Highscore software, and the crystal phase composition of the powder was identified by comparison with the powder crystal database of the International Diffraction Data Center (JCPDS-ICDD). X'pert Highscore software was employed to measure the crystallinity of the sample. Scanning electron microscopy (SEM) using JEOL-Ltd brand JSM-IT500LV was adopted to analyze the interior cross-section of ceramsite. The density of ceramsite was measured by MH-300A automatic solid densitometer. The compressive strength of the ceramsite was evaluated using the WDW-QT50 computer-controlled pellet pressure apparatus. The stress-time curve was selected, and the point at which the curve begins to decline sharply represents the maximum stress.

### 3 Results and discussion

### 3.1 Thermodynamics analysis

Thermodynamic calculations facilitate the rapid analysis of the viscosity of the complex systems [31] and guide the formation of the target phase [32]. Factsage is essential since it offers a sizable database that includes a range of computational functions for the chemical thermodynamics. Simultaneously, its diverse application templates provide tremendous

convenience for solving the corresponding problems [31–33]. In this study, the initial melting temperature and viscosity of the coal fly ash ceramsite composite system were analyzed using the Equilb module and viscosity module of Factsage, and the effects of formula and temperature on the surface state of the particles were elucidated. The phase diagram of the  $SiO_2$ - $Al_2O_3$ - $Fe_2O_3$ -CaO- $K_2O$ pure material system at different Fe<sub>2</sub>O<sub>3</sub> contents and sintering temperatures was drawn by the phase diagram module of Factsage [34]. Direct observations of the variations in distinct material phases generated at various sintering temperatures allowed for the determination of the content of each raw material component. Factsage's Equilb module was utilized to explore the transformation law of the liquid phase to the solid phase in the cooling process of raw materials D and E and determine the optimal content of each component.

### 3.1.1 Melting temperature and viscosity of system

The initial melting temperature varies for different formulas [33]. As indicated in Fig. 3(a), the initial melting temperatures of formulas A, B and C are not significantly different, while the initial melting temperatures of formulas D and E are significantly lower than that of the first three. The addition of potassium feldspar reduces the melting temperature of the system. In Fig. 3(b), the system viscosity of formulas A, B, C, D and E decreases significantly with increasing temperature. At 900–1300 °C, the system viscosity of formula E is higher than that of the other formulas, and that of formula B is the lowest.

## 3.1.2 Phase transformation of system at different sintering temperatures

Figure 4 illustrates the phase transition of formula D at different temperatures and ferric oxide contents. With the temperature increasing, the

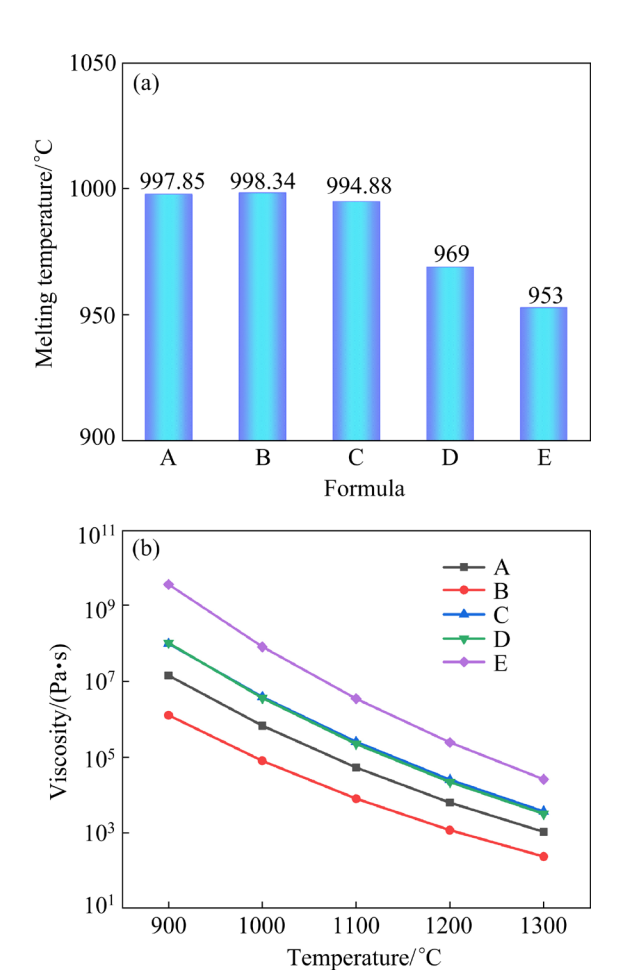
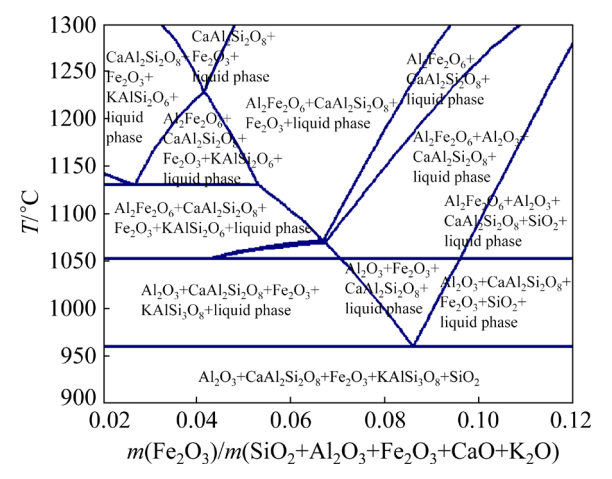


Fig. 3 Initial melting temperature (a) and viscosity variations (b) of different formulas



**Fig. 4** SiO<sub>2</sub>–Al<sub>2</sub>O<sub>3</sub>–Fe<sub>2</sub>O<sub>3</sub>–CaO–K<sub>2</sub>O phase diagram of formula D at different ferric oxide contents and sintering temperatures

liquid phase of formula D starts to be produced at The phase changes were analyzed longitudinally along the production point of the liquid phase [35]. The initial phases at room temperature are Al<sub>2</sub>O<sub>3</sub> (corundum), CaAl<sub>2</sub>Si<sub>2</sub>O<sub>8</sub> (anorthite), Fe<sub>2</sub>O<sub>3</sub> (hematite), KAlSi<sub>3</sub>O<sub>8</sub> (sanidine), and SiO<sub>2</sub> (tridymite). With the increase of temperature, KAlSi<sub>3</sub>O<sub>8</sub> (sanidine) and SiO<sub>2</sub> (tridymite) disappear, while the liquid phase appears. As the temperature continues to rise, parts of Al<sub>2</sub>O<sub>3</sub> (corundum) and Fe<sub>2</sub>O<sub>3</sub> (hematite) react to form Al<sub>2</sub>Fe<sub>2</sub>O<sub>6</sub>. When the temperature reaches 1200 °C, the final phase consists of Al<sub>2</sub>Fe<sub>2</sub>O<sub>6</sub>, CaAl<sub>2</sub>Si<sub>2</sub>O<sub>8</sub> (anorthite), and the liquid phase. The optimal formula ratio at each sintering temperature can be determined using the phase diagram of the relationship between the content of each oxide component and temperature.

### 3.1.3 Cooling process of phase separation

The precipitation of formula D phase during cooling at 1600 °C is shown in Fig. 5. From the liquid phase to the solid phase, hematite (Fe<sub>2</sub>O<sub>3</sub>) and Al<sub>2</sub>Fe<sub>2</sub>O<sub>6</sub> precipitate at about 1600 °C, anorthite (CaAl<sub>2</sub>Si<sub>2</sub>O<sub>8</sub>) precipitates at about 1500 °C, sanidine (KAlSi<sub>3</sub>O<sub>8</sub>) precipitates at about 1350 °C, corundum (Al<sub>2</sub>O<sub>3</sub>) precipitates at about 1330 °C, and tridymite (SiO<sub>2</sub>) precipitates at about 1000 °C. The transition from the solid phase to the liquid phase is depicted in the cooling crystallization phase diagram (Fig. 5). The relationship among the precipitation process, phase transition and viscosity of the cooling crystallization (Fig. 3) clearly explains the formation of large pores. The increase in system viscosity is mainly due to the presence of

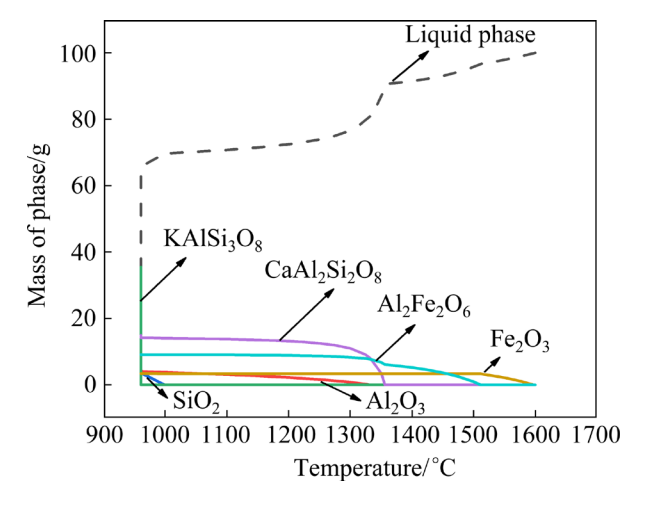


Fig. 5 Phase transition of formula D during high temperature cooling process

a mixed solid—liquid phase. At this phase, increasing the temperature is not conducive to the emission of gas, leading to the formation of large pores [36]. The expansion of ceramsite is explained further by this neat combination of thermodynamics and subsequent investigations.

### 3.2 Formula and process optimization design

3.2.1 Optimization of cooling mode: trying segmented cooling

The quality of ceramsite is significantly influenced by the cooling process. In general, a relatively reasonable cooling system for clay pellets is that the roasted pellets can be cooled quickly to 1000-700 °C after the expansion zone at the highest temperature. The temperature chosen for this study is 850 °C [35]. This work aims to enhance the expansion effect of the pellet by coordinating the changes in the surface viscosity and the reaction rate of pore-making in the firing process of the pellet. While the cooling technique of the pellet after fire changes, the formula of the basic materials mostly remains unchanged. The cooling mode was optimized from furnace cooling (Process 0) to segmented cooling (rapid cooling was adopted above 850 °C, and furnace cooling was adopted below 850 °C, Process 1).

Figure 6 compares the XRD patterns of slow cooling (A<sub>0</sub> sample) and segmented cooled (A<sub>1</sub> sample) ceramsite fired at 1200 °C. A raw material formula was supplemented with 83% of coal fly ash, 15% of quartz, and 2% of bentonite. After sintering at a high temperature of 1200 °C, A<sub>0</sub> was slowly cooled down to 850 °C, which was found to consist mainly of quartz, hematite, and mullite (Al<sub>6</sub>Si<sub>2</sub>O<sub>13</sub>) phases; Al<sub>6</sub>Si<sub>2</sub>O<sub>13</sub> was converted to Al<sub>4.95</sub>Si<sub>1.05</sub>O<sub>9.52</sub> (mullite) and (Na,Ca)Al(Si, Al)<sub>3</sub>O<sub>8</sub> (sodiumanhydrite intermediate) in stage cooling A<sub>1</sub>.

The average strength decreases from 6.78 to 5.07 kN, and the average density decreases from 2.28 to 2.15 g/cm $^3$  (Fig. 7). Figure 8 shows the

macroscopic morphology of the ceramsite under different formulas and processes.

3.2.2 Optimization of pore-making mode: adding pore-forming agent

It is challenging to obtain the appropriate expansion impact alone by altering the technique. Thus, the density of ceramsite would be reduced by adding a pore-forming agent. The effects of poreforming agent toner and silicon carbide on the expansion of coal fly ash-based ceramsite were investigated.

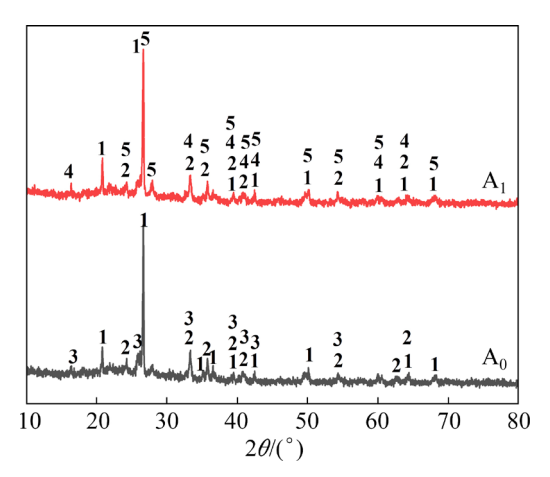


**Fig. 6** XRD patterns of  $A_0$  and  $A_1$  under different cooling systems:  $1-\text{SiO}_2$  (quartz);  $2-\text{Fe}_2\text{O}_3$  (hematite);  $3-\text{Al}_6\text{Si}_2\text{O}_{13}$  (mullite);  $4-\text{Al}_{4.95}\text{Si}_{1.05}\text{O}_{9.52}$  (mullite);  $5-\text{(Na, Ca)Al(Si, Al)}_3\text{O}_8$  (sodium-anorthite intermediate)

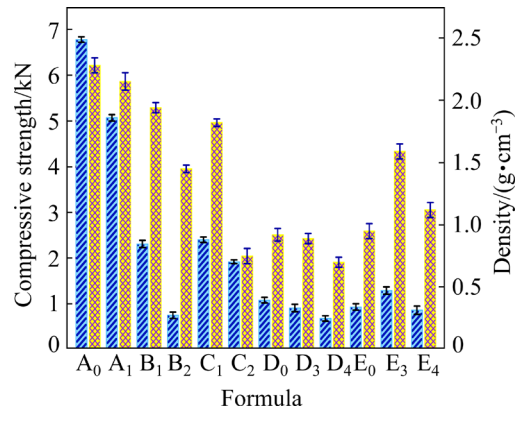


Fig. 7 Compressive strength and density of different formulas

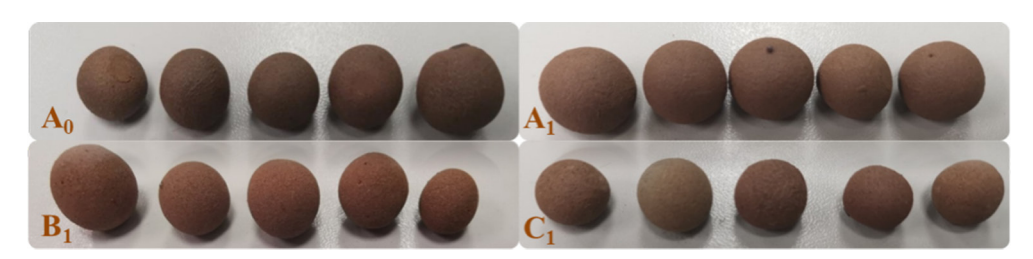


Fig. 8 Apparent morphology of ceramsite in different formulas

Under the constant condition (Process 1), the raw material formula was varied, and the physical phases and performance indices were compared for different raw material formulas (A, B and C in Tables 3 and 4).  $A_1$  mostly consists of quartz, hematite, Al<sub>4.95</sub>Si<sub>1.05</sub>O<sub>9.52</sub> (mullite), and (Na,Ca)Al-(Si,Al)<sub>3</sub>O<sub>8</sub> (sodium-anorthite intermediate). Despite the addition of pore-forming agent, B<sub>1</sub> still consists of quartz, hematite, Al<sub>4.95</sub>Si<sub>1.05</sub>O<sub>9.52</sub> (mullite), and (Na,Ca)Al(Si, Al)<sub>3</sub>O<sub>8</sub> (sodium-anorthite intermediate), with only slight variations observed among the phases. C<sub>1</sub> changes from Al<sub>4.95</sub>Si<sub>1.05</sub>O<sub>9.52</sub> (mullite) and  $(Na,Ca)Al(Si,Al)_3O_8$ (sodium-anorthite intermediate) to (Ca,Na)(Al,Si)<sub>2</sub>Si<sub>2</sub>O<sub>8</sub> (ordered natrium anorthite). Figure 7 suggests that the degree of crystallinity is directly correlated with the content of coal fly ash (Tables 3 and 4). Specifically, the higher content of coal fly ash leads to the lower crystallinity of the sample. The high-temperature sintered coal fly ash was amorphous and the raw material particles were not remelted. The ceramsite samples formed are the result of the adhesion between particles at high temperatures.

The average strengths of  $A_1$ ,  $B_1$ , and  $C_1$  are 5.07, 2.31, and 2.40 kN, respectively. The respective average densities of  $A_1$ ,  $B_1$  and  $C_1$  are 2.15, 1.94 and 1.82 g/cm<sup>3</sup> (Fig. 7). With the addition of a pore-forming agent, the overall density of ceramsite decreased significantly and underwent slight swelling with a corresponding decrease in strength. SiC has the best pore-forming properties when compared to agents on  $B_1$  and  $C_1$ , whereas  $C_1$  offers

a lower density and higher strength than  $B_1$ . Thus, SiC pore-forming agent is fairly stable.

The impact of cooling mode and various pore-forming agents on the expansion morphology of ceramsite is depicted in Fig. 8. According to the appearance morphology of ceramsite, segmented cooling  $A_1$  and slow cooling  $A_0$  have not much difference. The overall performance of  $C_1$  is superior than  $B_1$  with the addition of SiC; however, the apparent morphology of ceramsite is not readily discernible. Figure 9 shows the different phases in their XRD patterns  $(A_1, B_1, \text{ and } C_1)$ 

3.2.3 Optimization of roasting method: increasing heating rate

Without altering the process, exclusively adding a pore-forming agent reduces the density of the final product while the corresponding compressive strength decreases. Therefore, the effect on ceramsite can be achieved by varying the heating mechanism. This study examined the effects of rapid heating under formulas B and C on the expansion impact of coal fly ash-based ceramsite (Table 3). Under formula B, the ceramsite was preheated at 400 °C shortly before it was removed from the furnace, which was then heated to 1100 °C (Process 1). Once the temperature reached 1200 °C, the ceramsite was then placed into the furnace to further heating (Process 2). The same procedure was performed for B and C. Process 1 and Process 2 adopted the cooling system of rapid cooling above 850 °C and the cooling system of furnace cooling below 850 °C.

**Table 3** Mineral phase content of mixtures for formula (wt.%)

Serial number	Coal fly ash	Quartz	Bentonite	Potassium feldspar	Carbon powder	Silicon carbide
A	83	15	2	_	_	_
В	90	_	2	_	8	_
C	70	15	4	_	3	8
D	60	_	3	34	_	3
E	30	_	7	60	_	3

Table 4 Chemical composition of ceramsite formula (wt.%)

Serial number	$SiO_2$	$Al_2O_3$	$Fe_2O_3$	CaO	MgO	$K_2O$	Na <sub>2</sub> O	C	Others
A	54.48	17.88	11.20	2.01	0.95	1.42	1.44	3.98	10.62
В	42.73	19.34	12.14	2.18	1.03	1.53	1.57	12.32	19.48
C	61.48	15.86	9.44	1.69	0.80	1.27	1.22	8.76	8.24
D	54.59	18.70	8.46	1.53	0.80	3.95	1.87	_	10.10
E	58.61	17.84	4.70	0.86	0.54	5.78	1.98	_	9.69

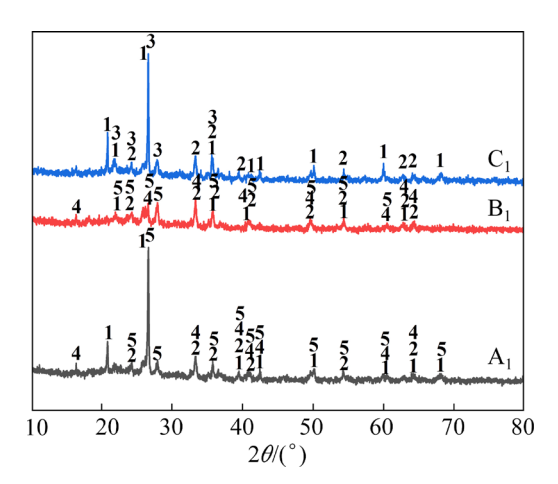


**Fig. 9** XRD patterns of A<sub>1</sub>, B<sub>1</sub> and C<sub>1</sub> at different levels of pore-forming agent: 1–SiO<sub>2</sub> (quartz); 2–Fe<sub>2</sub>O<sub>3</sub> (hematite); 3–(Ca, Na)(Al, Si)<sub>2</sub>Si<sub>2</sub>O<sub>8</sub> (ordered natrium anorthite); 4–Al<sub>4.95</sub>Si<sub>1.05</sub>O<sub>9.52</sub> (mullite); 5–(Na,Ca)Al-(Si,Al)<sub>3</sub>O<sub>8</sub> (sodium–anorthite intermediate)

Figure 10 compares the XRD patterns of ceramsite under slow heating (B<sub>1</sub> and C<sub>1</sub>) and rapid heating (B<sub>2</sub> and C<sub>2</sub>). B<sub>1</sub> is composed of quartz, hematite, Al<sub>4.95</sub>Si<sub>1.05</sub>O<sub>9.52</sub> (mullite), and (Na,Ca)Al-(Si,Al)<sub>3</sub>O<sub>8</sub> (sodium-anhydrite intermediate). After rapid heating, B<sub>2</sub> is transformed from quartz,  $Al_{4.95}Si_{1.05}O_{9.52}$  (mullite), and  $(Na,Ca)Al(Si,Al)_3O_8$ (sodium-anhydrite inter mediate) to Na<sub>0.71</sub>K<sub>0.29</sub>Al-Si<sub>3</sub>O<sub>8</sub> (anorthoclase) and Al<sub>6</sub>Si<sub>2</sub>O<sub>13</sub> (mullite). C<sub>1</sub> is composed of quartz, hematite, and (Ca,Na)-(Al,Si)<sub>2</sub>Si<sub>2</sub>O<sub>8</sub> (ordered natrium anorthite). Rapid heating causes C<sub>2</sub> to transform from (Ca,Na)-(Al,Si)<sub>2</sub>Si<sub>2</sub>O<sub>8</sub> (ordered natrium anorthite) into Al<sub>4.95</sub>Si<sub>1.05</sub>O<sub>9.52</sub> (mullite). The heating process of the samples affects their crystallinity, which falls off with fast heating.

The average compressive strength decreases considerably from 2.31 kN of B<sub>1</sub> to 0.75 kN of B<sub>2</sub> and from 2.40 kN of C<sub>1</sub> to 1.92 kN of C<sub>2</sub>. The average density decreases from 1.94 g/cm<sup>3</sup> of B<sub>1</sub> to 1.45 g/cm<sup>3</sup> of B<sub>2</sub> and 1.82 g/cm<sup>3</sup> of C<sub>1</sub> to 0.75 g/cm<sup>3</sup>

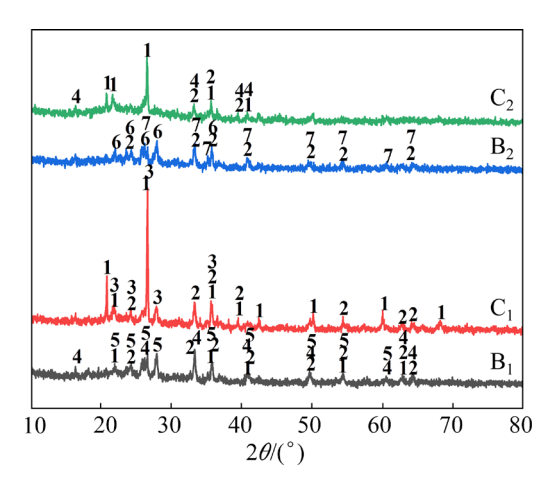


**Fig. 10** XRD patterns of  $B_1$ ,  $C_1$  and  $B_2$ ,  $C_2$  at different heating mechanisms:  $1-SiO_2$  (quartz);  $2-Fe_2O_3$  (hematite);  $3-(Ca,Na)(Al,Si)_2Si_2O_8$  (ordered natrium anorthite);  $4-Al_{4.95}Si_{1.05}O_{9.52}$  (mullite);  $5-(Na,Ca)Al(Si,Al)_3O_8$  (sodium—anorthite intermediate);  $6-Na_{0.71}K_{0.29}AlSi_3O_8$  (anorthoclase);  $7-Al_6Si_2O_{13}$  (mullite)

of C<sub>2</sub> (Fig. 7). Following rapid heating, the density and compressive strength of ceramsite significantly decrease.

The macroscopic graphic demonstrates that fast heating would cause the sample to expand. However, the surface became rough and cracked, and the shape turned irregular. Figure 11 depicts the morphology of ceramsite under various roasting techniques.

Roasting is one of the key factors that affect the sintering of ceramsite. The expansion effect in B<sub>2</sub> and C<sub>2</sub> is good when quick heating is used, and ceramsite typically causes a large number of fractures or even ruptures during the sintering process (Fig. 11). Specifically, the ceramsite surface fails to form a surface tension that encloses the escaping gas owing to its small viscosity. The strength of ceramsite diminishes as a result of these fissures. However, when the ceramsite particles are slowly cooled down in the furnace, they remain

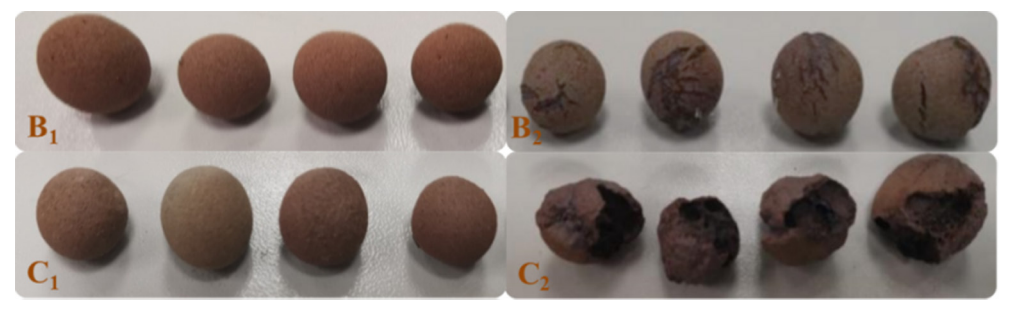


Fig. 11 Apparent morphology of ceramsite in different processes

intact, and the expansion effect is common in  $B_1$  and  $C_1$  (Fig. 11). The findings demonstrate that quick heating increases the expansibility of ceramsite, although the strength is not very great and the surface is rough and broken. Thus, corresponding measures should be taken to improve the appearance.

### 3.2.4 Formula optimization

The combination of pore-forming agents and process variations can significantly reduce the density and compressive strength of ceramsite. Therefore, further improvement is needed to obtain satisfactory samples. In this study, formulas D and E were used independently to investigate the effects of the fluxing agent and on the expansion of the coal fly the heating rate ash-based ceramsite (Table 3).

Typical fluxing agents contain Na<sub>2</sub>O, K<sub>2</sub>O, CaO, MgO, and FeO/Fe<sub>2</sub>O<sub>3</sub>, which reduces the melting temperature of ceramsite. According to formula D, the rapid heating system was adopted. After preheating at 400 °C, the ceramsite particles were removed and placed back when the temperature in the furnace reached 1050 °C (Process 3). After preheating at 400 °C, the ceramsite particles were gathered and added when the temperature in the furnace was increased to 1100 °C (Process 4). Process 3 and Process 4 employed the system of rapid cooling above 850 °C and furnace cooling below 850 °C.

The XRD patterns of D<sub>3</sub>, D<sub>4</sub>, E<sub>3</sub> and E<sub>4</sub> are contrasted in Fig. 12. After rapid heating at 1050 °C, D<sub>3</sub> is composed of quartz, hematite, Na<sub>0.71</sub>K<sub>0.29</sub>-AlSi<sub>3</sub>O<sub>8</sub> (anorthoclase), and Mg<sub>0.7</sub>Fe<sub>0.23</sub>Al<sub>1.97</sub>O<sub>4</sub>. After rapid heating at 1100 °C, D<sub>4</sub> changes from Na<sub>0.71</sub>K<sub>0.29</sub>AlSi<sub>3</sub>O<sub>8</sub> (anorthoclase) and Mg<sub>0.7</sub>Fe<sub>0.23</sub>-Al<sub>1.97</sub>O<sub>4</sub> to (Na,K)Si<sub>3</sub>AlO<sub>8</sub> (disordered anorthoclase) and (Mg,Fe)<sub>2</sub>SiO<sub>4</sub> (spinel olivine containing low iron). After rapid heating at 1050 °C, E<sub>3</sub> is mostly made up of hematite and KAlSi<sub>3</sub>O<sub>8</sub> (microcline). After rapid heating at 1100 °C, E<sub>4</sub> still consists of the same two minerals, but their contents change slightly.

Between  $D_3$  and  $D_4$ , the average compressive strength drops from 0.91 to 0.68 kN, and from  $E_3$  to  $E_4$  it decreases from 1.29 to 0.86 kN. The average density decreases from 0.89 g/cm<sup>3</sup> of  $D_3$  to 0.70 g/cm<sup>3</sup> of  $D_4$  and from 1.59 g/cm<sup>3</sup> of  $E_3$  to 1.12 g/cm<sup>3</sup> of  $E_4$  (Fig. 7). This finding demonstrates that the density and compressive strength of

ceramsite are not significantly affected by the temperature change during the first fast heating.

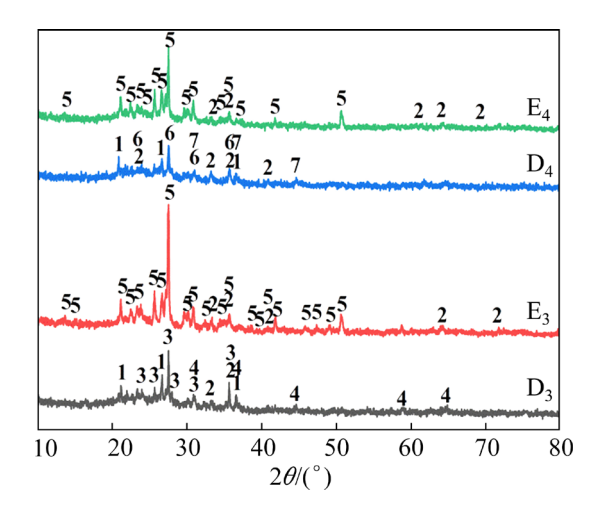


**Fig. 12** XRD patterns of D<sub>3</sub>, E<sub>3</sub> and D<sub>4</sub>, E<sub>4</sub> at various roasting processes: 1–SiO<sub>2</sub> (quartz); 2–Fe<sub>2</sub>O<sub>3</sub> (hematite); 3–Na<sub>0.71</sub>K<sub>0.29</sub>AlSi<sub>3</sub>O<sub>8</sub> (anorthoclase); 4–Mg<sub>0.7</sub>Fe<sub>0.23</sub>-Al<sub>1.97</sub>O<sub>4</sub>; 5–KAlSi<sub>3</sub>O<sub>8</sub> (microcline); 6–(Na,K)Si<sub>3</sub>AlO<sub>8</sub> (disordered anorthoclase); 7–(Mg,Fe)<sub>2</sub>SiO<sub>4</sub> (spinel olivine containing low iron)

### 3.3 Optimal product characterization

The use of a pore-forming agent, a fluxing agent, and quick heating will subsequently assist the expansion to some amount and decrease the density in line with the formula and process design in Section 3.2. Meanwhile, the corresponding strength also decreases. Particularly after the quick heating, the surface of the ceramsite shows noticeable fissures, failing to perform as intended. In this study, D and E (Table 3) were investigated without changing the process (slowly heating at 400–1200 °C, then slowly cooling to room temperature in the furnace, Process 0).

Figure 13 compares the XRD patterns of  $D_0$  with those of  $E_0$ . Quartz, hematite, and KAlSi<sub>3</sub>O<sub>8</sub> (microcline) phases make up the majority of  $D_0$ , while hematite and KAlSi<sub>3</sub>O<sub>8</sub> (microcline) phases comprise the majority of  $E_0$ . Crystallinity is highly determined by the content of coal fly ash. In particular, the crystallinity of system decreases when the coal fly ash concentration increases. As the coal fly ash content of D is about twice that of E, the crystallinity of D is significantly lower than that of E.

The average strength of  $D_0$  (1.08 kN) is slightly larger than that of  $E_0$  (0.93 kN); the average density of  $D_0$  (0.92 g/cm<sup>3</sup>) is marginally lower than

that of  $E_0$  (0.95 g/cm<sup>3</sup>) (Fig. 7). The macro figure shows that  $D_0$  has a superior expansion impact compared to  $E_0$ .

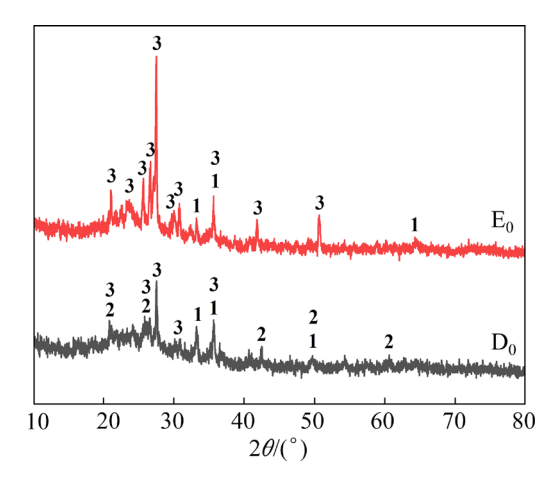


**Fig. 13** XRD patterns of D<sub>0</sub> and E<sub>0</sub>: 1–Fe<sub>2</sub>O<sub>3</sub> (hematite); 2–SiO<sub>2</sub> (quartz); 3–KAlSi<sub>3</sub>O<sub>8</sub> (microcline)

The apparent morphology of D<sub>4</sub> resembles that of B<sub>2</sub> and C<sub>2</sub> in Fig. 10, and both exhibit surface cracking that causes ceramsite deformation. During the rapid heating process, the gas produced will have a strong force to break the liquid phase on the surface, causing cracking. By comparing the apparent morphology of ceramsite (Fig. 14) with the data analysis (Fig. 13), the expansion process of ceramsite is a dynamic process, in which the expanding gas escapes into where it is surrounded by the liquid phase with appropriate viscosity. For expanded ceramsite to be prepared with outstanding performance and a pleasing appearance, dynamic equilibrium must be achieved. Through the comparative experiments, the formula and process of the final optimized product are determined as the combination of formula D and Process 0 (D<sub>0</sub>).

In light of the aforementioned investigations,  $D_0$  is chosen as the optimal product. The macrostructure of  $D_0$  is compared with that of commercially available ceramsite (Fig. 15). When products are burned with coal fly ash, the pores

almost all have the same regular shapes and distribution. Meanwhile, numerous large pores of commercially available ceramsite are available, with irregular shapes and uneven distribution.

Point scanning is performed at different points on the cross-section of D<sub>0</sub> and commercially available ceramsite, respectively (Fig. 16). The scanning results are analyzed as follows. In D<sub>0</sub> (Fig. 16(a)), where the oxide composition is homogenous, Spot 1 is dispersed around several tiny holes with a rough surface. Al<sub>2</sub>O<sub>3</sub> has the highest concentration, followed by MgO molten oxide (Fig. 17(a)). Aluminum and silicon content only slightly vary from one another, and the amount of molten elements is likewise quite small (Fig. 17(b)). Spot 3 is located in the inner wall of the pore and is relatively smooth. The molten oxide content is relatively high, and the contents of SiO<sub>2</sub> and Al<sub>2</sub>O<sub>3</sub> are similar (Fig. 17(a)). The findings show that silicon and aluminum content differ significantly, although the content of molten components is essentially the same (Fig. 17(b)). Spot 2 in commercially available ceramsite is distributed around large pores, with a rough surface. Spot 3 is located on the connected phase which has a smooth surface. A detailed explanation was added for the formation of large pores in the SEM images. During high-temperature sintering, the liquid content in the ceramsite rises as its viscosity falls, and the gas produced in the system is more concentrated, which overcomes the surface tension of liquid phase and gives rise to large pores.

Figure 17 was obtained by converting each element in  $D_0$  and commercially available ceramsite into oxides based on the point and surface scanning electron microscopy. At various locations of the  $D_0$  segment, oxide concentration varies noticeably, as seen in Fig. 17(a). At various locations along the cross-section,  $SiO_2$  is distributed in a rather homogeneous manner. Figure 17(b) indicates that the distribution of elements at different positions of

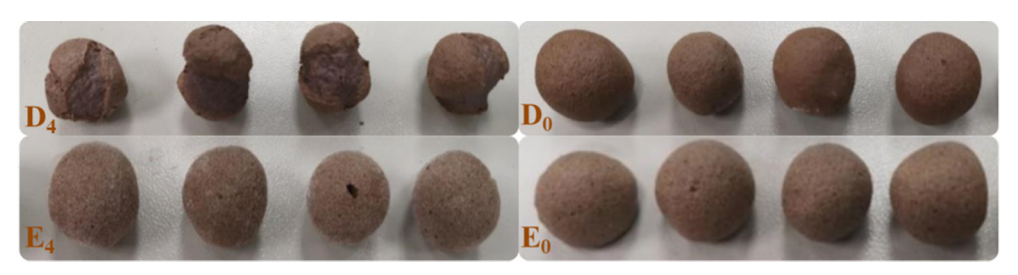


Fig. 14 Apparent morphology of ceramsite in different formulas and processes

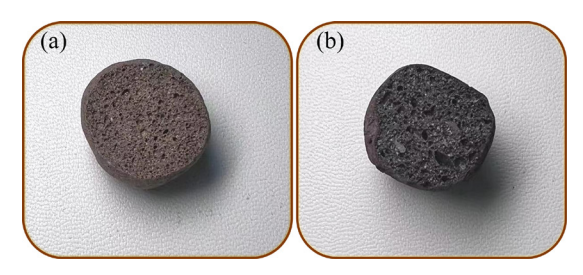


Fig. 15 Macrostructure of cross-section of  $D_0$  (a) and commercial ceramsite (b)

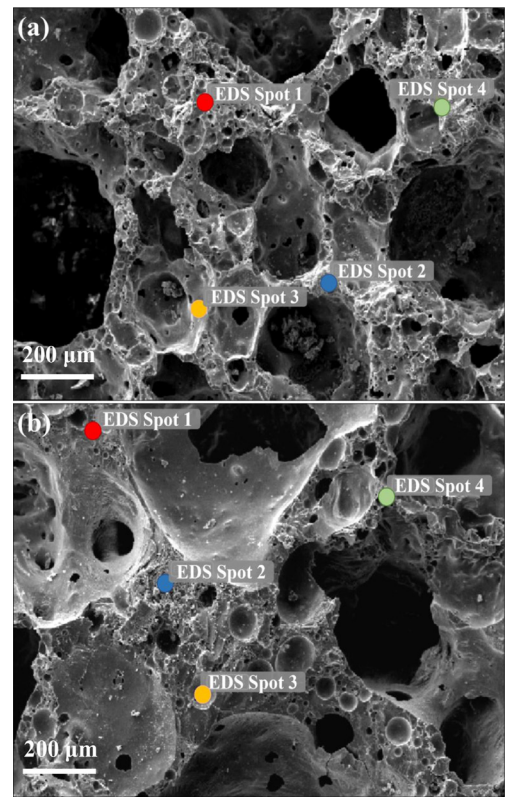


Fig. 16 Point-scan micrographs of cross-section of  $D_0$  (a) and commercial ceramsite (b)

section  $D_0$  is roughly the same, and Si and Al at different points of the cross-section account for over 80% of the total elements.

The skeleton linked phase of D<sub>0</sub> is subjected to plane scanning (Fig. 18). The distribution of O, Al, Si, Fe and Ca is illustrated as follows. The skeleton is a product generated by the fusion of several atoms with varied distributions and contents, according to the chemical formula analysis. Oxygen is the most abundant element and usually combines with other elements to form oxides, including silicon, aluminum, and iron. Furthermore, Fig. 18(f) clearly illustrates the calculation results for crystal phase precipitation during cooling. Anorthite (CaAl<sub>2</sub>Si<sub>2</sub>O<sub>8</sub>) is an example of a Ca-containing solid

phase that precipitates as a solid phase after cooling as opposed to a homogeneous molten phase, creating a comparatively concentrated form of Ca that is not uniformly distributed.

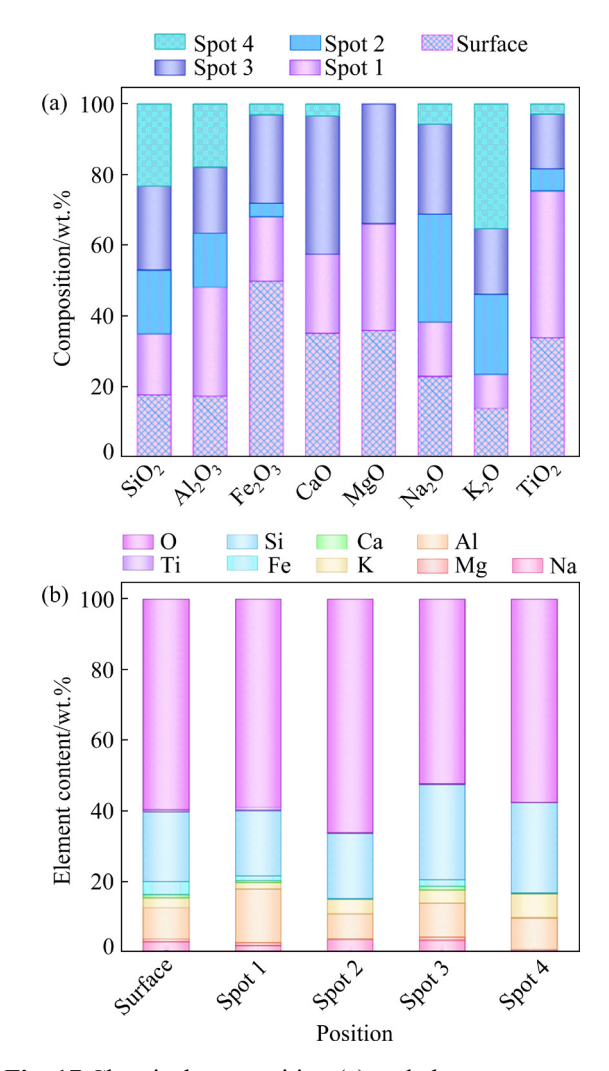


Fig. 17 Chemical composition (a) and element content of each point (b) on surface of  $D_0$ 

### 4 Conclusions

- (1) The viscosity of five formula systems was examined from a thermodynamics standpoint using Factsage software. The viscosity decreases with increasing initial melting temperature. The viscosity increase in the system could be primarily caused by the existence of a solid–liquid mixed phase, in which the temperature increase is not conducive to gas discharge, resulting in the formation of large pores.
- (2) There is a certain correlation between the strength of ceramsite and the cooling processes. The overall density of ceramsite remains essentially

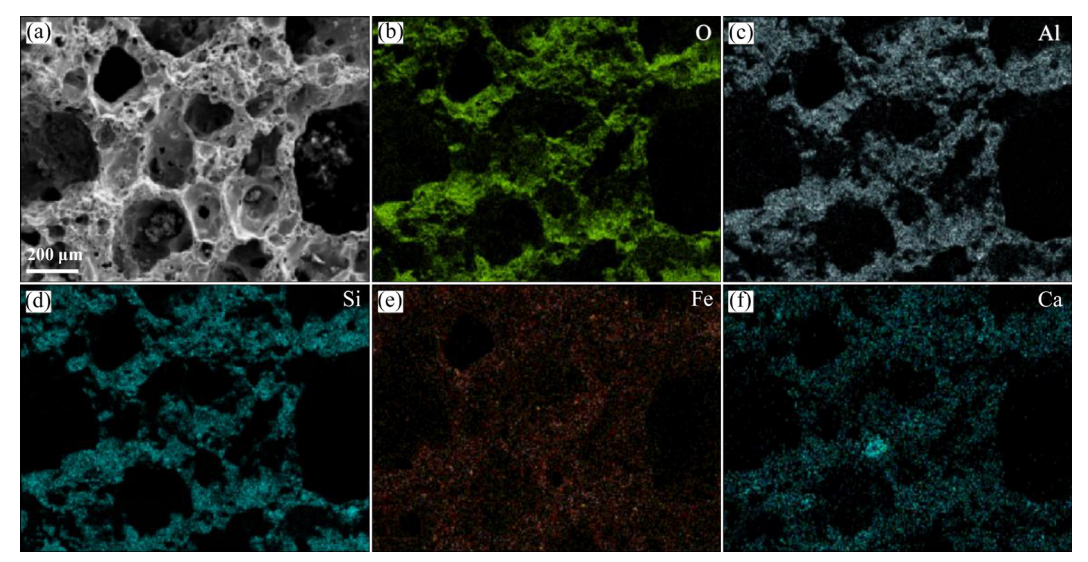


Fig. 18 Surface scanning microstructure of cross section of D<sub>0</sub>

similar with the addition of C and SiC to the formula, but the strength is significantly decreased. The density and strength of ceramsite are considerably reduced by rapid heating. The sample expanded significantly, but the surface became rough and cracked, with an irregular shape. As a result, rapid warming is not conducive to the requirement of having a smooth ceramsite surface.

(3) To produce lightweight and high-strength ceramsite based on high-dosage coal fly ash, we created an optimal path and process that controlled the cooling technique, pore-forming agent, heating method, and formula. Formula D was ultimately found to be the optimal formula. The roasting temperature was 1200 °C, and the holding period was 5 min. The density of the ceramsite particles produced was less than 0.93 g/cm³, and the strength was up to 1.08 kN. The specific strength of ceramsite was significantly higher than that of several products purchased randomly in the market.

### **Acknowledgments**

This study is supported by the National Key Research and Development Program of China (No. 2020YFC1909202), the Postdoctoral Foundation of China (Nos. BX20200389, 2020M672513), and the National Natural Science Foundation of China (No. 52004343)

### References

[1] CHAI Chun-jing, SONG Hui-ping, FENG Zheng-jun, ZHANG Jin-cai, CHENG Fang-qin. Research progress on

- the fly ash ceramsite [J]. Clean Coal Technology, 2020, 26(6): 15–26. (in Chinese)
- [2] CHEN Zhao, ZUO Xu-jun, YANG Ben-hong, YANG Pan-pan, ZHOU Xin. Preparation of porous ceramics with fly ash as main raw material [J]. Journal of Anhui Jianzhu University, 2017, 25(4): 38–42. (in Chinese)
- [3] LIU Chun-li, MA Shu-hua, DING Jian, LUO Yang, ZHENG Shi-li, ZHANG Yi. Kinetics of decomposition of mullite and corundum in coal fly ash under highly alkaline condition [J]. Transactions of Nonferrous Metals Society of China, 2019, 29(4): 859–867.
- [4] QIN Juan, CUI Chong, CUI Xiao-yu, HUSSAIN A, YANG Chuan-meng. Preparation and characterization of ceramsite from lime mud and coal fly ash [J]. Construction and Building Materials, 2015, 95: 10–17.
- [5] NGUYEN T B T, CHATCHAWAN R, SAENGSOY W, TANGTERMSIRIKUL S, SUGIYAMA T. Influences of different types of fly ash and confinement on performances of expansive mortars and concretes [J]. Construction and Building Materials, 2019, 209: 176–186.
- [6] LUO Yang, WANG Jian-yu, WU Ying-hong, LI Xiao-yan, CHU P K, QI Tao. Substitution of quartz and clay with fly ash in the production of architectural ceramics: A mechanistic study [J]. Ceramics International, 2021, 47(9): 12514–12525.
- [7] ZHANG Wei, GU Jia-rui, ZHOU Xu, LI Yong, WANG Ya-guang, XUE Yang, LIU Xiao-ming. Circulating fluidized bed fly ash based multi-solid wastes road base materials: Hydration characteristics and utilization of SO<sub>3</sub> and f-CaO [J]. Journal of Cleaner Production, 2021, 316: 128355.
- [8] DONG Rong. Comprehensive utilization of fly ash [J]. Journal of Green Science and Technology, 2020, 16: 90–95. (in Chinese)
- [9] LUAN Hao-xiang, WU Jin, ZHU Wan-xu, PAN Jia-yu, ZHANG Rui-dong, ZHOU Hong-mei. Preparation and acoustic performance of recycled ceramsite concrete noiseabsorbing plate [J]. Journal of Central South University (Science and Technology), 2020, 51(5): 1299–1308.

- [10] JIANG Zhou-qing, YANG Jing, MA Hong-wen, WANG Le, MA Xi. Reaction behaviour of Al<sub>2</sub>O<sub>3</sub> and SiO<sub>2</sub> in high alumina coal fly ash during alkali hydrothermal process [J]. Transactions of Nonferrous Metals Society of China, 2015, 25(6): 2065–2072.
- [11] HAMMEL E C, IGHODARO O L R, OKOLI O I. Processing and properties of advanced porous ceramics: An application based review [J]. Ceramics International, 2014, 40(10): 15351–15370.
- [12] YANG Jie, LIU Xue-ying. Progress on the preparation of ceramsite [J]. Building Energy Efficiency, 2013, 41(267): 45–47
- [13] LI Liang. Experimental study on preparation of fly ash ceramsite [J]. Bulletin of the Chinese Ceramic Society, 2017, 36(5): 1577–1589.
- [14] CAO Shi-wei, CHEN Wei, JING Zhao-qian. Phosphorus removal mechanism in constructed wetlands with high calcium fly ash as substrate [J]. Journal of Central South University (Science and Technology), 2012, 43(12): 4939–4943. (in Chinese)
- [15] WANG Shao-feng, SUN Li-cheng, HUANG Lin-qi, LI Xiao-bing, SHI Ying, YAO Jin-rui, DU Shao-lun. Non-explosive mining and waste utilization for achieving green mining in underground hard rock mine in China [J]. Transactions of Nonferrous Metals Society of China, 2019, 29(9): 1914–1928.
- [16] LIU Shu-xian, SHEN Li-li, NIU Fu-sheng. Researching status and prospect of lightweight aggregates obtained from solid wastes in China [J]. Advanced Materials Research, 2010, 163/164/165/166/167: 624–628.
- [17] LIU Sen, YANG Cong-ren, LIU Wei, YI Long-sheng, QIN Wen-qing. A novel approach to preparing ultra-lightweight ceramsite with a large amount of fly ash [J]. Frontiers of Environmental Science & Engineering, 2020, 14(4): 1–11.
- [18] CHENG Gong, LI Qiong-hui, SU Zhan, SHENG Sheng, FU Jie. Preparation, optimization, and application of sustainable ceramsite substrate from coal fly ash/waterworks sludge/ oyster shell for phosphorus immobilization in constructed wetlands [J]. Journal of Cleaner Production, 2018, 175: 572–581.
- [19] CHOO T F, MOHD SALLEH S M, KOK K Y, MATORI K, RASHID S A. A study on the utilization of coal fly ash derived grog in clay ceramics [J]. Materials (Basel), 2020, 13(22): 1–12.
- [20] KOTOVA O B, IGNATIEV G V, SHUSHKOV D A, HARJA M, BROEKMANS M A T M. Preparation and properties of ceramic materials from coal fly ash [M]. Minerals: Structure, Properties, Methods of Investigation, 2020: 101–107.
- [21] GUO Yan-qing. Comprehensive utilization of fly ash [J]. Energy and Energy conservation, 2020, 4: 140-1. (in Chinese)
- [22] MAHMOUDI S, SRASRA E, ZARGOUNI F. Preparation, qualities and defects of ceramic materials from Tunisian clay minerals [J]. Surface Engineering and Applied Electrochemistry, 2017, 53(3): 295–301.
- [23] HOU Li-jun, LIU Tao-yong, LU An-xian. Red mud and fly

- ash-based ceramic foams using starch and manganese dioxide as foaming agent [J]. Transactions of Nonferrous Metals Society of China, 2017, 27(3): 591–598.
- [24] ZHANG Lan, ZHANG Long, DONG Xiang, ZHANG Song, ZHAO Yan, CEN Qi-hong, ZHANG Kao-min. The effect and mechanism of Si/Al ratio on microstructure of zeolite modified ceramsite derived from industrial wastes [J]. Microporous and Mesoporous Materials, 2021, 311: 110667.
- [25] YAO Shuai-feng, XU Hong-liang, SUN Jun-min, MIAO Wen-bo. Preparation of porous ceramics using highaluminum fly ash [J]. Journal of Synthetic Crystals, 2019, 48(4): 687–692. (in Chinese)
- [26] WANG Qing-gang, HUANG Jian-feng, PAN Li-min, LIU Yi-jun, LI Jia-yin, HUANG Ling-yan. Preparation and properties of lightweight porous ceramics based on fly ash [J]. Bulletin of the Chinese Ceramic Society, 2017, 36(12): 4130–4134. (in Chinese)
- [27] WU Li-fan, LI Tao, XI Lei, HAN Qiang, MA Yong-lin, XING Shu-qing. Study on preparation of fly ash porous ceramics and rare earth modification [J]. Non-Metallic Mines, 2020, 43(6): 21–24. (in Chinese)
- [28] GAO Xia, LIANG Shuo-yang, FENG Yun-kang, WANG Xin-quan, YI Gui-lan, SHI Yong-lin, ZHANG Mei, GUO Min. Foundamental experimental study on preparation of permeable brick by fly ash [J]. Environmental Engineering, 2019, 37: 297–300. (in Chinese)
- [29] YAO Z, T, JI X, S, SARKER P, K, TANG J H, GE L Q, XIA M S, XI Y Q. A comprehensive review on the applications of coal fly ash [J]. Earth-Science Reviews, 2015, 141: 105–121.
- [30] DAO Bing-xiang, ZHANG Jing-wen, XI Dan-li. Application of fly ash mixed with electroplating sludge and activated suldge manufacture ceramsite [C]//2009 International Conference on Energy and Environment Technology, 2009: 198–202.
- [31] ROCHA V C, SILVA M L, BIELEFELDT W V, VILELA A C F. Assessment of viscosity calculation for calcium-silicate based slags using computational thermodynamics [J]. REM-International Engineering Journal, 2018, 71(2): 243–252.
- [32] WANG Shao-han, LUO Xian, JIN Hui-xin. Preparation of imitation basalt compound based on thermodynamic calculation [J]. Materials (Basel), 2019, 12(20): 1–11.
- [33] ZHANG Wen-juan, WANG Cheng-yan, MA Bao-zhong. Leaching kinetics of calcium molybdate with hydrochloric acid in presence of phosphoric acid [J]. Transactions of Nonferrous Metals Society of China, 2019, 29(4): 859–867.
- [34] MAGDZIARZ A, GAJEK M, NOWAK-WOŹNY D D, WILK M. Mineral phase transformation of biomass ashes— Experimental and thermochemical calculations [J]. Renewable Energy, 2018, 128: 446–459.
- [35] MAO Xi-shuang. Preparation and calcination mechanism of light-weight shale ceramisite [D]. Nanning: Guangxi University, 2006. (in Chinese)
- [36] MA Long, LI Guo-zhong. Influence of sintering temperature on performance of red mud lightweight ceramsite [J]. Advanced Materials Research, 2013, 662: 323–326.

### 高掺量粉煤灰制备轻质高强陶粒

王莉莎 1,2, 王艳秀 1,2, 孙 伟 1,2, 王成文 1,2, 孟祥松 1,2

- 1. 中南大学 资源加工与生物工程学院,长沙 410083;
- 2. 战略含钙矿产资源清洁高效利用湖南省重点实验室,长沙 410083

摘 要:提出一种从粉煤灰中制备高强轻质陶粒的方法,为粉煤灰的贮存和有效利用粉煤灰中  $SiO_2$ 、 $Al_2O_3$ 等有用物质提供一种潜在的解决方案。在热力学分析的基础上,结合复杂硅酸盐体系中的矿物转化,对冷却方法、焙烧工艺和原料配方进行改进,设计出高掺量(60%-90%,质量分数)粉煤灰烧结制备轻质高强陶粒的优化方法。在焙烧温度为 1200 °C、保温时间 5 min 的条件下,得到密度小于 0.93 g/cm³、强度高达 1.08 kN 的陶粒。用该方法制备的陶粒比强度明显高于市场上随机购买的几种陶粒产品。

关键词: 热力学; 矿物转型; 过程控制; 固体废弃物利用; 陶粒; 粉煤灰

(Edited by Xiang-qun LI)